Journal of Applied Geophysics 139 (2017) 291–305

Contents lists available at ScienceDirect

Journal of Applied Geophysics

journal homepage: www.elsevier.com/locate/jappgeo

Quantification of tracer plume transport parameters in 2D saturated porous media by cross-borehole ERT imaging

G. Lekmine [a,b,d,*], H. Auradou [b,c], M. Pessel [a], J.L. Rayner [d]

[a] Laboratoire GEOPS, Univ. Paris-Sud, Orsay F-91405, France
[b] Laboratoire FAST, Univ. Paris Sud, CNRS, Univ. Paris-Saclay, F-91405 Orsay, France
[c] CNRS, Orsay F-91405, France
[d] CSIRO Land and Water, Private Bag No. 5, Wembley, WA 6913, Australia

ARTICLE INFO

Article history:
Received 19 June 2016
Received in revised form 1 January 2017
Accepted 21 February 2017
Available online 27 February 2017

Keywords:
Cross-borehole ERT imaging
Tracer test experiments
Groundwater contaminant
Transport in porous media

ABSTRACT

Cross-borehole ERT imaging was tested to quantify the average velocity and transport parameters of tracer plumes in saturated porous media. Seven tracer tests were performed at different flow rates and monitored by either a vertical or horizontal dipole-dipole ERT sequence. These sequences were tested to reconstruct the shape and temporally follow the spread of the tracer plumes through a background regularization procedure. Data sets were inverted with the same inversion parameters and 2D model sections of resistivity ratios were converted to tracer concentrations. Both array types provided an accurate estimation of the average pore velocity v_z. The total mass M_{tot} recovered was always overestimated by the horizontal dipole-dipole and underestimated by the vertical dipole-dipole. The vertical dipole-dipole was however reliable to quantify the longitudinal dispersivity λ_z, while the horizontal dipole-dipole returned better estimation for the transverse component λ_x. λ and M_{tot} were mainly influenced by the 2D distribution of the cumulated electrical sensitivity and the Shadow Effects induced by the third dimension. The size reduction of the edge of the plume was also related to the inability of the inversion process to reconstruct sharp resistivity contrasts at the interface. Smoothing was counterbalanced by a non-realistic rise of the ERT concentrations around the centre of mass returning overpredicted total masses. A sensitivity analysis on the cementation factor m and the porosity ϕ demonstrated that a change in one of these parameters by 8% involved non negligible variations by 30 and 40% of the dispersion coefficients and mass recovery.

1. Introduction

The understanding of contaminant fate in groundwater environments is of high interest for supply and management of water resources in urban areas. Contaminant releases infiltrate through the soil to cross the vadose zone and reach the water table where they spread following the particular flow directions and hydrodynamic conditions of groundwater bodies. Localisation and monitoring of contaminants is the first important step to remediation procedures (Meyer et al., 1994; Herrera and Pinder, 2005). However, accurate information are usually constrained by the lack of density of sampling locations which are representative of the vicinity of the boreholes but do not render of local heterogeneities and preferential flow directions of the plumes (Kim and Lee, 2007).

Electrical resistivity Tomography (ERT) is a non-destructive geophysical method allowing to scan in 1D to 3D, from surface or downhole measurements, the subsurface to provide valuable information about electrical properties of soils and aquifers. Borehole ERT imaging was initially used for hydrogeological investigations to obtain complementary information about groundwater flow and heterogeneities from tracer test injections (Bevc and Morrison, 1991; Slater et al., 1997) or to monitor remediation procedures (Daily and Ramirez, 1995; Labrecque et al., 1996b). However, the integrative character of the method do not allow to recover sharp conductive interfaces (Loke and Barker, 1996), which coupled to the non-uniqueness of the inverse modelling solution limits the interpretation to qualitative estimations (Binley et al., 1996; Ramirez et al., 2005; Wilkinson et al., 2010). During the last decades, research studies focused on testing the abilities of ERT to quantify contaminant or solute transport parameters. Time-lapse inversion procedures based on simultaneous, differenced or background regularization were developed to characterize the temporal resistivity variations attributed to tracer resistivity changes through petrophysical relationships (Daily et al., 1995; Day-Lewis et al., 2002; Hayley et al., 2011; Perri et al., 2012). Numerical and field tests demonstrated that cross-borehole measurements were the most appropriate to reconstruct the contours of tracer plumes (Bing and Greenhalgh, 2000; Chambers et al., 2007; Oldenborger et al., 2007a, 2007b). These previous studies showed that the type of array and the sequence of measurements greatly influenced the shape and intensity of the resistivity contrasts attributed to tracer temporal spreads (Rucker, 2014; Bellmunt et al., 2016). Laboratory

* Corresponding author at: Laboratoire GEOPS, Univ. Paris-Sud, Orsay F-91405, France.
E-mail address: gregory.lekmine@csiro.au (G. Lekmine).

http://dx.doi.org/10.1016/j.jappgeo.2017.02.024
0926-9851/

experiments were also performed on soil columns to evaluate the potential of ERT imaging to quantify solute transport from tracer conductivity breakthrough curves (Binley et al., 1996; Slater et al., 2002). The inversion processes, and particularly the smoothness constrained methods, generally overestimated the extent of contaminant plumes and underpredicted the actual concentrations present in groundwater (Oldenborger et al., 2007b). More controlled experimental procedures were developed to quantify transport parameters of tracers from 3D–ERT acquisitions (Singha and Gorelick, 2006; Koestel et al., 2008). Complementary works also tested the response of ERT imaging on transport parameters for high and low flow regimes (Koestel et al., 2009a), or soil types to quantify lateral mixing (Koestel et al., 2009b), or aimed to characterize preferential flows in heterogeneous media (Garré et al., 2010; Meyerhoff et al., 2014; Wehrer and Slater, 2015). They highlighted that the use of petrophysical relationships such as Archie's law introduced supplementary errors, leading to wrong estimates of the total mass and dispersivities extracted from the breakthrough curves. These experimental studies provided great information on the possibilities and drawbacks of ERT imaging to quantify solute transport parameters. Though, uncertainties remained due to the shape and spatial distribution of tracers plumes coupled to small scale structural heterogeneities. This usually leads to inaccuracies in quantifying the sensitivity of transport properties by ERT imaging.

The objective of this study was to determine the main parameters influencing the quantification of solute transport from cross-borehole ERT imaging under controlled 2D flow conditions. First, experiments were developed in 2D small scale porous media to monitor the propagation of tracer plumes by a high-resolution camera while cross-borehole ERT measurements were performed. We chose to focus the tests on the response of two standard measurement sequences to confirm the reliability of ERT to recover average pore velocities, dispersion parameters and total masses of the injected tracers. The methodology applied to evaluate these transport parameters from ERT measurements is then described. We finally provide a short discussion about the main uncertainties inferred by the measurement protocols, the inversion strategy and the petrophysical parameters influencing the recovery of the tracer transport parameters.

2. Experimental procedures

2.1. 2D experimental design

The experimental design was developed to optimize the 2D characteristics of the hydrodynamic properties and the ERT acquisitions. The tests were performed in a transparent plexiglass container of dimension 27.5 cm high × 8.5 cm long × 1 cm thick, to favor longitudinal and transverse hydrodynamic conditions while the transport properties were negligible in the third dimension (Fig. 1). In the bottom, the inlet was covered with a permeable 350 μm nylon screen mesh to ensure water flow while preventing loss of fine material particles from the container. The container was incrementally filled with glass beads ranging from 400 to 500 μm in diameter with an average value $d_p = 420$ μm small enough to avoid flow channelling on the walls (Charette et al., 2007). A particular packing procedure was followed before each experiment to minimize structural arrangements. Once fully packed, the top outlet was sealed with 3 injectors connected to a syringe pump to impose a constant vertical water flow. The porosity was estimated before each test by weight difference of the container between dried and full water saturation of the bead pack. The average porosity was estimated to $\phi = 0.36 \pm 0.01$ for a total pore volume $PV = 84.2$ mL. The permeability and the hydraulic conductivity estimated using Kozeny-Carman relation (Guyon et al., 2001) were respectively $k = 1.8 \times 10^{-10}$ m^2 and $K_w = 1.1 \times 10^{-3}$ m/s. The container was then placed between a light panel and a high-resolution video camera (400 × 1002 pixels). Two vertical lines of 21 of stainless brass electrodes with a minimum spacing of 1 cm were screwed on both sides of the container to create a 2D ERT acquisition plane centred in the 3rd dimension of the medium. The first and last electrodes of each line were respectively located 3.75 cm from the inlet and outlet to reduce horizontal boundary effects (Fig. 1).

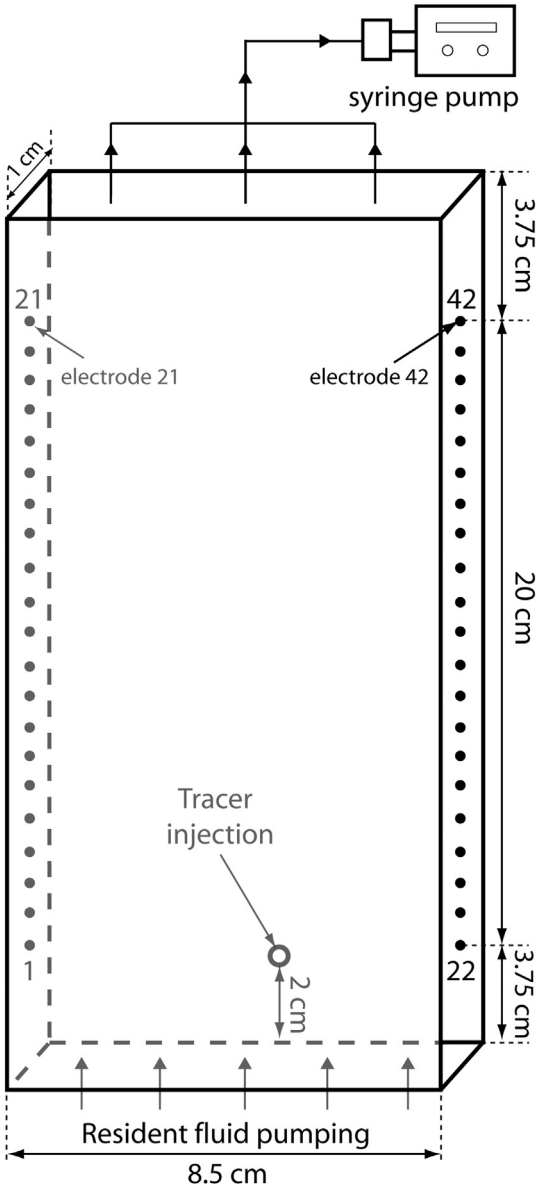

Fig. 1. Schematic view of the 2D laboratory experiments. Dots on both sides represent the two vertical lines of electrodes. The white circle represents the tracer injection point localised at X = 4.25 cm, Y = 0.5 cm and Z = −25.5 cm.

Table 1
Fluid and flow properties for 2D laboratory experiments 1 to 7.

Exp.	Array type	Resident fluid				Dyed tracer		
		C_r [g/L]	σ_r [μS/cm]	Q_{pump} [mL/min]	v_{pump} [cm/min]	C_t [g/L]	σ_t [μS/cm]	Vol_t [mL]
1	Horizontal	0.3	630	0.75	0.25	0.75	1583	11
2	Horizontal	0.3	630	1.5	0.5	0.75	1583	11
3	Horizontal	0.3	630	3.0	1.0	0.75	1583	11
4	Vertical	0.3	638	0.75	0.25	0.75	1583	11
5	Vertical	0.3	638	1.5	0.5	0.75	1583	11
6	Vertical	0.3	638	3.0	1.0	0.75	1583	11
7	Vertical	0.3	638	2.0	0.65	0.75	1583	11

2.2. Experimental procedure

A total of 7 experiments were performed at 3 different flow rates and 2 types ERT acquisition sequences (Table 1). Before each experiment, the pore space was initially saturated with CO_2 to favor dissolution of entrapped air during the establishment of water saturation. Water saturation was established by dipping the bottom of the container into a tank filled with the resident fluid made of demineralised water containing $C_r = 0.3$ g/L of NaCl (Fig. 1). The fluid was vertically pumped at a slow flow rate $Q = 0.25$ mL/min to ensure full saturation. The pump was then stopped and a first picture was taken while a sequence of ERT measurements ρ_a^{t0} was acquired at $t = 0$. The flow was re-established at constant Q_{pump} (Table 1) while 11 mL of a dyed tracer were punctually injected from the centre of the bead pack, 2 cm above the inlet at

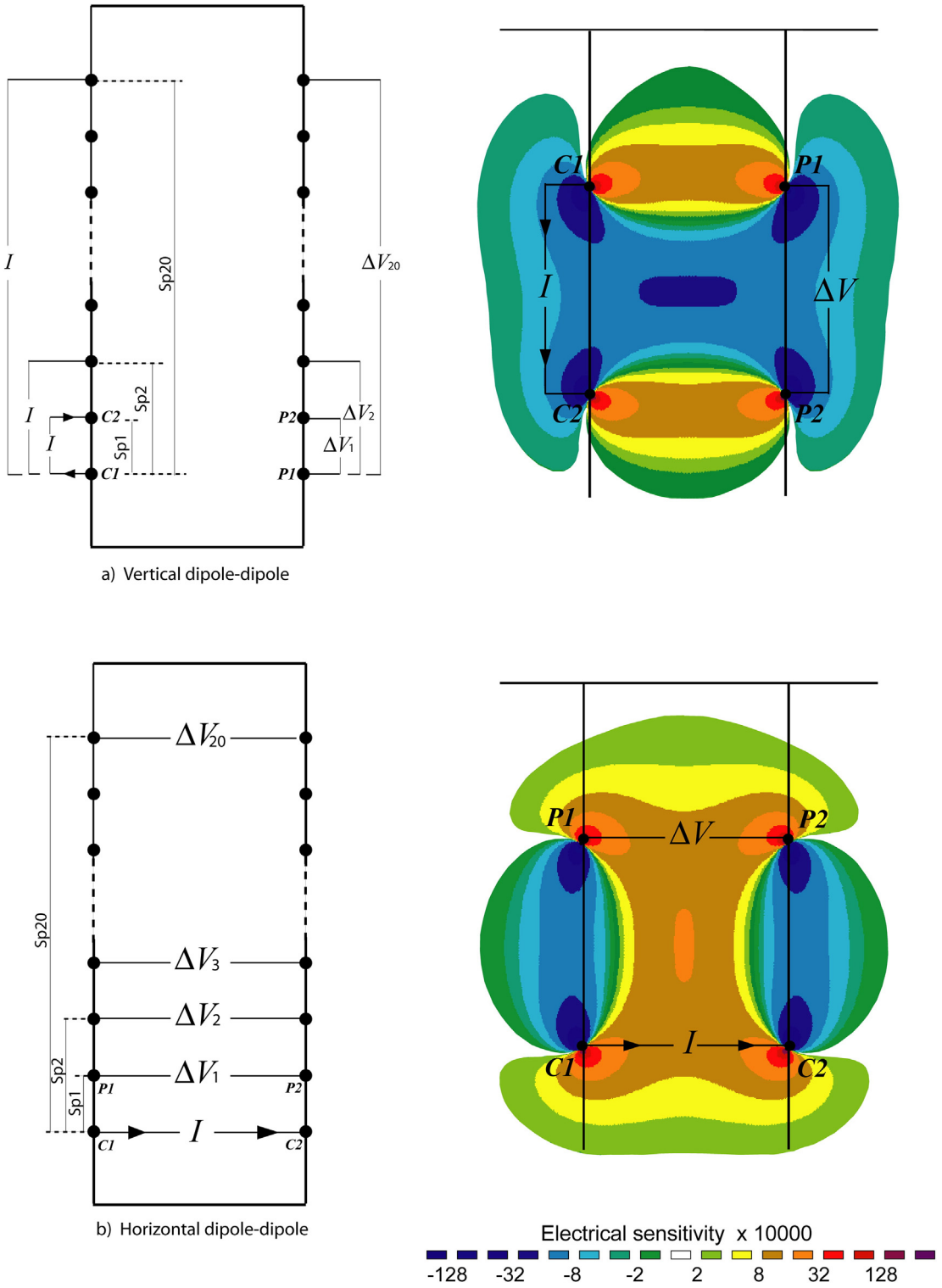

Fig. 2. Measurement sequences for the selected quadripoles in vertical (a) and horizontal (b) dipole-dipole and associated sensitivity distributions for a single quadripole calculated by the Fréchet derivatives for a 2D homogeneous synthetic half-space. With *C1C2* the current electrode pair, *P1P2* the potential electrodes, *I* [A] the injected current, *ΔV* [V] the measured potentials, and spacing Sp1 = 1 cm, Sp2 = 2 cm, Sp20 = 20 cm.

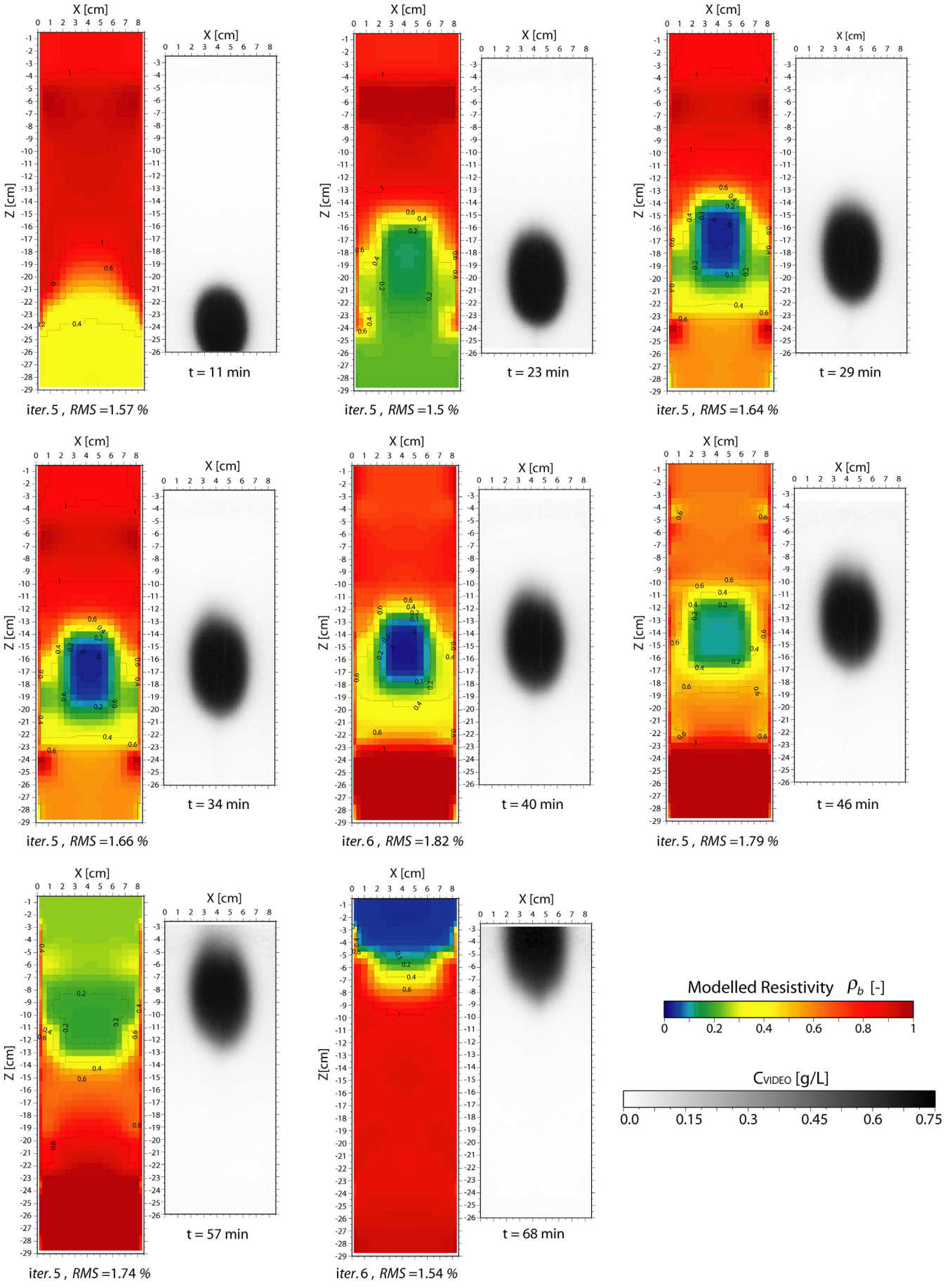
X [cm]
Z [cm]
t = 11 min
iter. 5 , RMS =1.57 %
t = 23 min
iter. 5 , RMS =1.5 %
t = 29 min
iter. 5 , RMS =1.64 %
t = 34 min
iter. 5 , RMS =1.66 %
t = 40 min
iter. 6 , RMS =1.82 %
t = 46 min
iter. 5 , RMS =1.79 %
t = 57 min
iter. 5 , RMS =1.74 %
t = 68 min
iter. 6 , RMS =1.54 %
Modelled Resistivity ρ_b [-]
0 0.2 0.4 0.6 0.8 1
CVIDEO [g/L]
0.0 0.15 0.3 0.45 0.6 0.75

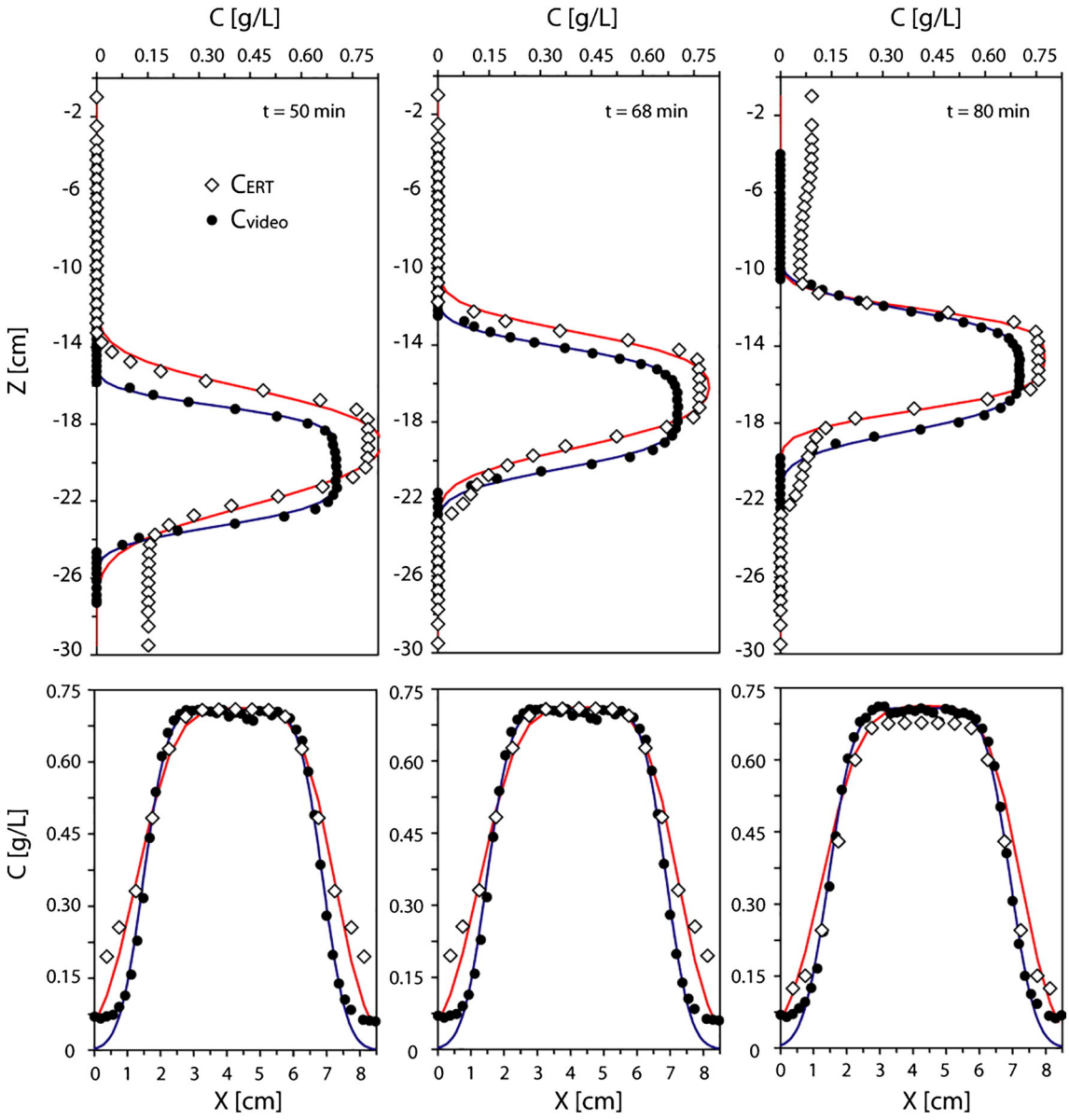

Fig. 4. Longitudinal and transverse tracer breakthrough curves extracted from experiment 1 and adjusted by Eq. (14). C_{ERT} and C_{VIDEO} are horizontally averaged for $3.75 < x_p < 5.25$ and vertically around $z_p \pm 0.5$ cm.

0.75 mL/min. The injection lasted for 14.5 min to ensure longitudinal and transverse extension of the plume over the characteristic length of the porous medium in the third dimension (i.e 1 cm). The tracer contained 0.75 g/L of NaCl and 0.05 g/L of methyl blue (Table 1). During the experiments, pictures were acquired every 30 s and ERT sequences were repeated until the dyed tracer plume crossed the full height of the bead pack. For each picture acquired by the video camera, the relative tracer concentrations in each pixel were obtained from a polynomial adjustment of the light absorption:

$$C_{VIDEO}(x,z) = \frac{b_1 A(x,z) + b_2 A^2(x,z) + b_3 A^3(x,z)}{b_1 A0(x,z) + b_2 A0^2(x,z) + b_3 A0^3(x,z)} \quad (1)$$

with $A(x,z)$ the light absorbance at time t for the pixel of coordinates (x,z), $A0(x,z)$ the absorbance measured at $t = 0$, before the injection of the blue dye and $b_1 = 0.186$, $b_2 = 0.0087$, $b_3 = 0.108$ were calibration parameters. Factors b_1, b_2 and b_3 were determined by plotting the averaged light absorbance of the porous media saturated by a fluid containing a known amount of dye as a function of its concentration.

2.3. ERT measurement configuration

The choice of the ERT measurement sequence is an important step to accurately retrieve the resistivity contrasts attributed to the temporal spread of the tracer plume. Previous studies developed sensitivity analysis strategies based on local and global optimization approaches to select the most appropriate sequences (Furman et al., 2004, 2007). Cross-borehole configurations present better signal to noise ratios and the highest sensitivities in-between boreholes (Bing and Greenhalgh, 2000; Wilkinson et al., 2008). Similarly to Bellmunt et al. (2016), the

Fig. 3. 2D model sections of bulk resistivity ρ_b obtained from inversion of regularised data $\rho_{a_n}^t$ for experiment 2 with a L_2-norm applied to the data misfit. Grey level maps show the dye concentration fields obtained from the video analysis. C_{VIDEO} were renormalised to vary on the same range of the ERT concentrations C_{ERT}.

best strategy would require for each time step to select the quadripoles showing the highest sensitivities in the area of the centre mass of the plume. However, in field conditions this procedure assumes to obtain detailed and reliable prior information on the shape and temporal propagation of the tracer. We considered here that no prior information were available in terms of acquisition strategy and chose to test the reliability of two standard sequences of horizontal (experiments 1 to 3) and vertical (experiments 4 to 7) cross-borehole arrays covering the whole domain in the 2D plane of the electrode lines. These two configurations were previously successfully used to localize and monitor the shape and expansion of the tracer resistivity contrasts due to saline tracer migration between boreholes (Oldenborger et al., 2007a, 2007b). In the vertical configuration, the current was injected in one borehole and the measurements were acquired symmetrically with the same spacing on the other side (Fig. 2a). For the horizontal sequence, the current was injected through the medium while potential differences ΔV were measured consecutively with an increasing spacing up to the top, then *C1C2* moved up by 1 cm and a new set of ΔV were acquired above the current electrodes (Fig. 2b). For a single quadripole in a homogeneous half-space, both arrays present the same range of absolute sensitivity with high values in the centre part of porous medium where the tracer plumes were localised. However, the vertical dipole-dipole presents horizontal distribution of the sensitivity while horizontal dipole-dipole sensitivity contrasts are distributed vertically. Then the number of electrodes and the minimum spacing (Sp1 = 1 cm) were chosen in respect of the dimensions of the container and the distance between boreholes to cover the entire area of the medium and maximize the 2D electrical sensitivity in the centre part. For both arrays, a sequence of 210 measurements was acquired on each time step, in the flow direction from the bottom to the top of the bead pack. Data acquisition was automated using a Syscal Pro connected to the electrodes through a multiplexer, for each measurement a constant voltage $V_{ab} = 12$ V was maintained for 250 ms between the current pair of electrodes and prior to the current injection a self-potential measurement was performed and removed from the electrical potential. This led to the complete acquisition of the 210 measurements in 6 min considered as the total length of a time-step. This temporal resolution was necessary to minimize motion blur and temporal aliasing due to the spread of the tracer plume, affecting the quantification of the transport parameters and total mass recovery (Rucker, 2014). The sequence was repeated until the tracer plume fully crossed the outlet on top of the porous medium.

Reciprocal error measurements were collected during background acquisition to estimate data quality. Each measurement was repeated 4 times returning standard deviations lower than 1% for all the background measurements performed in vertical dipole-dipole (experiments 4 to 7 in Table 1) and 205 measurements of the horizontal dipole-dipole sequence (experiments 1 to 3). The 5 remaining quadripoles, with the largest electrode spacing between the current and electrode pairs, presented standard deviations varying from 2 to 5%. During the experiments each measurement was also repeated 4 times, standard deviations increased over time steps but these were not significant as it remained under 4% for all quadripoles except the 5 measurements previously cited which increased up to 70%. These measurements were particularly noise sensitive due to their low electrical sensitivity. They were included in the inverse modelling procedure with a low weight in the data weighting matrix W_d (Eq. (6)).

3. Data treatment and inversion procedure

3.1. Background regularization to tracer concentrations

The edges of the container strongly enhanced the values of measured apparent resistivities, screening the modelled temporal resistivity variations attributed to dispersion and transport of the tracers. To overcome these boundary effects a background regularization of the measured apparent resistivities ρ_a^t, was performed for each time step (Daily et al., 1995; Nimmer et al., 2008):

$$\rho_{an}^{\ t} = \frac{\rho_a^t}{\rho_a^{t0}} \tag{2}$$

where ρ_{an}^t [Ω·m] is the normalised apparent resistivity for a quadripole configuration at time t and ρ_a^{t0} [Ω·m] is the corresponding background measurement acquired at $t = 0$ before the injection.

Inversion of the regularised data sets, ρ_{an}^t, produced 2D discretised model sections of bulk resistivities ρ_b in each pixel of coordinates (x,z) (Fig. 3). They can be linked to the local fluid conductivity $\sigma_f(x,z)$ [S/m] through the formation factor (Archie, 1942):

$$\frac{\sigma_f(x,z)}{\sigma_b(x,z)} = \frac{\phi^{-m}}{Se^n} \tag{3}$$

where $\sigma_b(x,z) = 1/\rho_b(x,z)$ is the local modelled bulk conductivity in [S/m], the porosity $\phi = 0.36$ and the water saturation $Se = 1$ were constant. The saturation index n did not have any influence since the medium was fully water saturated. The cementation factor $m = 1.3$ was chosen from previous studies performed with glass beads on similar ranges of porosity (Archie, 1942).

Eq. (3) was then constant over the course of the experiment and the temporal changes of $\sigma_b(x,z)$ were only attributed to local variations in NaCl concentrations (Fig. 3). In these conditions, the ERT resident concentration $C_{ERT}(x,z)$ [mg/L] in tracer for each cell of the models is given by (Binley et al., 1996; Koestel et al., 2008):

$$\frac{C_{ERT}(x,z) - C_r}{C_t - C_r} = \frac{\sigma_f(x,z) - \sigma_r}{\sigma_t - \sigma_r} \tag{4}$$

$$C_{ERT}(x,z) = \frac{\sigma_b(x,z)\phi^{-m} - \sigma_r}{\sigma_t - \sigma_r}(C_t - C_r) + C_r \tag{5}$$

where σ_r and σ_t [S/m] are respectively the initial conductivity of the resident fluid and the saline tracer (Table 1).The glass bead surface conductivity was not considered in Eq. (3) because of the low Dukhin number, $\varepsilon = 0.08$, showing that the surface conductivity was negligible compared to resident fluid conductivity (Revil and Glover, 1998; Leroy et al., 2008). Although the laboratory experiments were well constrained

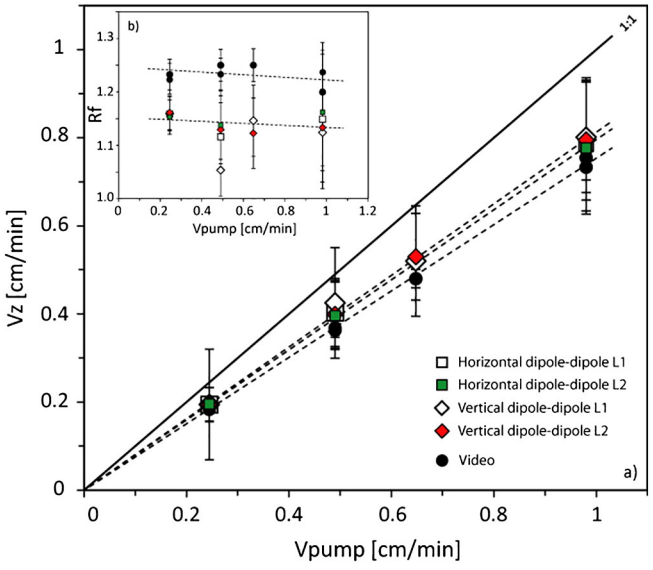

Fig. 5. Vertical average velocities v_z in a) obtained from linear fitting of the vertical position of the centre of mass of the plume $z_p = v_z.t$ (Eq. (14)) as function of time. In b) associated retardation factors R_f estimated from the ratio v_{pump}/v_z for experiments 1 to 7. L_1 and L_2 refer to the type of norm applied to the data misfit vector (Eq. (6)).

through the establishment of ϕ and *Se*, uncertainties remained in the value of *m*.

3.2. Inversion procedure

Data sets of ρ_{an}^{t} (Eq. (2)) were inverted with Res2Dinv (Loke, 2004) considering 3D current flow but 2D distribution of the resistivity contrasts. The inversion procedure is based on the Gauss-Newton method applied to a smoothness-constrained least-square inversion (Labrecque et al., 1996a). Models were iteratively optimized by finite-element recalculation of the electrical potential fields through the Poisson's equation. The estimation of the parameter vector m^k for iteration *k* was calculated according to the method described in Loke and Barker (1996) by minimizing the objective function φ:

$$\varphi\left(m^{k+1}\right) = \left\| W_d\left[d-h\left(m^k\right)\right]^T\left[d-h\left(m^k\right)\right]\right\|^n + \alpha\left\|\left(m^k-m^0\right)^T.W_p\left(m^k-m^0\right)\right\|^n \quad (6)$$

where $h(m^k)$ is the modelled data vector from model parameters at iteration *k*, m^0 is the vector of reference model parameters taken as the average value of the data set *d*. W_d and W_p are the data weighting and regularization matrices, *n* is the norm applied to each vector and α the damping factor controlling the step of the variation parameter vector Δm^k:

$$\Delta m^k = \left[J^T J + \alpha W_p\right]^{-1}\left[J^T W_d\left(d-h\left(m^k\right)\right)-\alpha W_p\left(m^k-m^0\right)\right] \quad (7)$$

where *J* is the Jacobian matrix of the partial derivatives. The sensitivity of the norms and inversion parameters (Eqs. (6) & (7)) as well as the choice of the grid mesh size greatly influences the estimated dispersion parameters (Lekmine et al., 2012). The 2D grid dimension was 8.5 × 30 cm containing a total of 1026 cells (19 × 54) with a squared mesh size of 0.5 cm. The mesh was vertically refined to 0.25 cm on both vertical sides in contact with the electrodes to reduce artefacts due to sharp resistivity changes. Coarser and refiner meshes were also tested but the 19 × 54 grid was the best compromise to minimize over smoothing of the tracer plume contours, reduce modelling

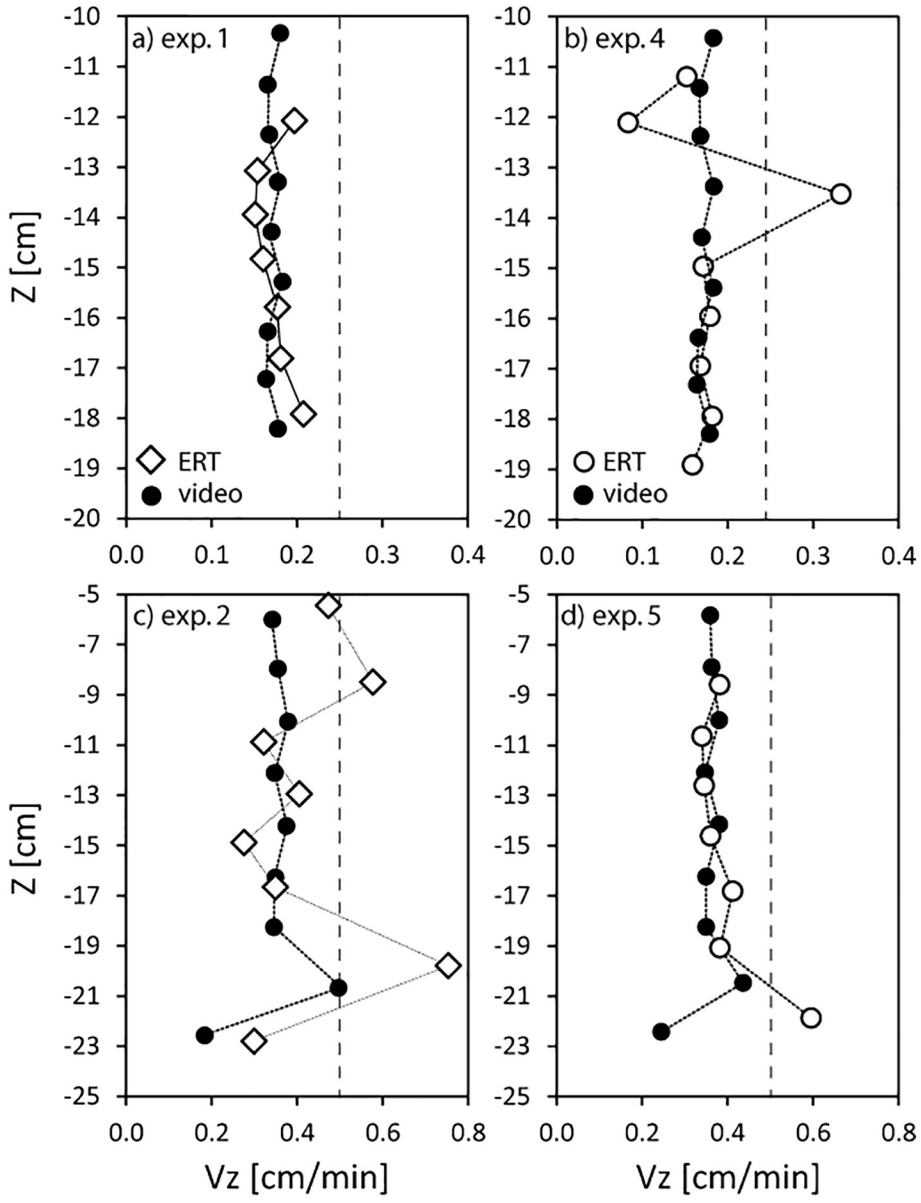

Fig. 6. Vertical relative velocity v_z as function of Z estimated from each temporal concentration curve fitted with Eq. (14) for data acquired in horizontal dipole-dipole in a) and c), and vertical dipole-dipole in b) and d). Filled circles represent the corresponding video analysis and vertical dashed lines show the pump velocity v_{pump}.

artefacts in areas less constrained by the data and ensure full recovery the longitudinal and transverse spatial breakthrough curves for the 7 experiments (Fig. 4). Neumann's boundary conditions were imposed on borehole edges while Dirichlet's conditions were applied to the bottom inlet and top outlet. We chose to test the robustness of the inversion by running the modelling procedure twice, with a L_1 ($n = 1$) and L_2 ($n = 2$) norms applied to the data misfit of the objective function. A L_1 norm was always maintained on the parameter misfit with an initial damping factor $\alpha = 0.1$ and a final value of 0.001. The logarithms of the normalised apparent resistivities were inverted, a maximum number of 7 iterations was chosen with recalculation of the Jacobian matrix J, and the reference model m^0 was the model produced at iteration 1.

3.3. Quantification of transport parameters and total mass

The physical processes that control the flux of the tracer are advection, hydrodynamic dispersion and adsorption on the particles. Adsorption was here fast, reversible and the mass of tracer absorbed varied linearly with the concentration. Transport was thus described by the following advection-diffusion equation:

$$R_f \frac{\partial C}{\partial t} = D_z \frac{\partial^2 C}{\partial z^2} - v_z \frac{\partial C}{\partial z} + D_x \frac{\partial^2 C}{\partial x^2} \tag{8}$$

where $R_f[-]$ is the retardation factor, D_z *and* D_x [m^2/s] are the longitudinal and transverse dispersion coefficients, v_z [m/s] is the vertical average pore velocity and C [kg/m^3] represents the C_{ERT} or C_{VIDEO} tracer concentration. The dispersion coefficients are here the sum of mechanical mixing and molecular diffusion such as:

$$D_{x,z} = \lambda_{x,z}.v_z + D_m \tag{9}$$

where D_m [m^2/s] is the molecular diffusion coefficient, λ_x and λ_z [m] are respectively the horizontal and vertical dispersivities. Eq. (9) becomes dimensionless by dividing by D_m:

$$\frac{D_{x,z}}{D_m} = \frac{\lambda_{x,z}}{d_p} Pe + 1 \tag{10}$$

where the Péclet number $Pe = v_z.d_p/D_m$ is the ratio of the tracer advection rate to its diffusion rate over the particle size. Longitudinal and transverse transport parameters were quantified from fitting C_{ERT} and C_{VIDEO} concentrations passing through the centre of mass of the tracer plume (Eqs. (1) & (5)) horizontally and vertically with a one dimensional volume-averaged solution. For our initial and boundary conditions, where $t_0 = 14.5$ min is the duration of the tracer injection:

$$C(z,0) = 0 \tag{11}$$

$$\frac{-D_z}{v_z}\frac{\partial C}{\partial z} + C\Big|_{z=0} = \begin{cases} C_t & 0 < t < t_0 \\ 0 & t > t_0 \end{cases} \tag{12}$$

$$\frac{\partial C}{\partial z}(\infty, t) = 0 \tag{13}$$

The solution of the advection-diffusion along the vertical axis is (Van Genuchten and Alves, 1982):

$$C(z,t) = \begin{cases} C_t \,.\, A(z,t) & 0 < t < t_0 \\ C_t \,.\, A(z,t) - C_t \,.\, A(z,t_0) & t > t_0 \end{cases} \tag{14}$$

with

$$A(z,t) = \frac{1}{2} erfc\left[\frac{R_f.z - v_z.t}{2(D_z.R_f.t)^{1/2}}\right] + \left(\frac{v_z^2.t}{\pi D_z.R_f}\right)^{1/2} exp\left[-\frac{(R_f.z - v_z.t)^2}{4D_z.R_f.t}\right] - \frac{1}{2}\left(1 + \frac{v_z.z}{D_z} + \frac{v_z^2.t}{D_z.R_f}\right) exp\left(\frac{v_z.z}{D_z}\right) erfc\left[\frac{R_f.z + v_z.t}{2(D_z.R_f.t)^{1/2}}\right]. \tag{15}$$

The solution in the horizontal direction $C(x,t)$ was obtained by setting $v_z = 0$ in Eq. (14).

For each time step vertical and horizontal breakthrough curves passing through the centre of mass of the plume (x_p, z_p) were respectively averaged horizontally over $3.75 < x_p < 5.25$ cm and vertically over 0.5 cm on both sides of z_p, and then adjusted by Eq. (14). Example of concentration curves and their adjustments by the analytical solution are shown in Fig. 4.

The total mass recovery M_{tot} was estimated for each time step by integrating C_{ERT} and C_{VIDEO} over the 400 × 1002 pixels of the images and the 1026 cells of the 2D discretised models (Oldenborger et al., 2007b; Koestel et al., 2009a):

$$M_{tot} = \phi \sum_{i=1}^{Ncell} C_i V_i \tag{16}$$

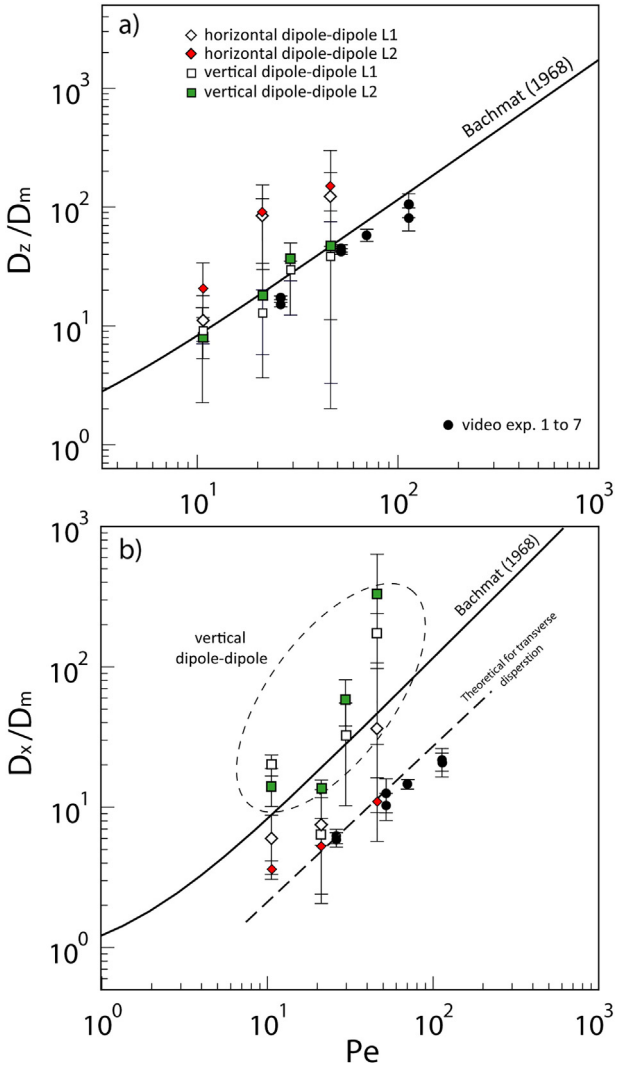

Fig. 7. Longitudinal (a) and transverse (b) dispersion coefficients estimated from ERT and video imaging as function of the Péclet number. Results are compared to the theoretical curve for longitudinal dispersion from Bachmat (1968). Coefficients are averages of the values obtained at each time step by adjusting the data with Eq. (14).

where V_i [m^3] is the total volume of the cell i determined from the full thickness of the bead pack. The relative concentrations C_{VIDEO} were renormalised on the NaCl concentration ranges to be compared to C_{ERT} in Fig. 9 and M_{tot} in Fig. 11. The use of the 2.5D forward modelling strategy described in part 3.2 may contribute to create modelling artefacts and prevent to retrieve the actual resistivity contrasts when 3D structures such as boreholes or 3D tracer plumes are present (Nimmer et al., 2008). This could have an influence on the total mass recovered M_{tot}, however we assumed that these effects were negligible for the particular experimental conditions of this study, where the 2D tracer plume was localised in the plane between both electrode vertical lines. Then the mass attributed to each image cell of the model was calculated under the assumption that the tracer mass distribution was homogeneous in the third dimension.

4. Results

4.1. Electrical recovery of the plume contours

Fig. 3 presents the 2D inversion results of the regularised data for 8 selected time-steps of experiment 2 for measurements acquired with the horizontal dipole-dipole sequence (Table 1). Models were selected at the 5th and the 6th iteration for which the RMS was <2%. Each resistivity section was compared to the corresponding renormalised 2D concentrations of the dyed-tracer obtained by the video analysis. At $t =$ 11 min, the punctual injection of the tracer was still occuring at $Z = -24.5$ cm with a bulk resistivity ratio $\rho_b = 0.4$ expressing a local resistivity depletion by 60% compared to the background measurements. From top to $Z = -19$ cm, models show constant and homogeneous

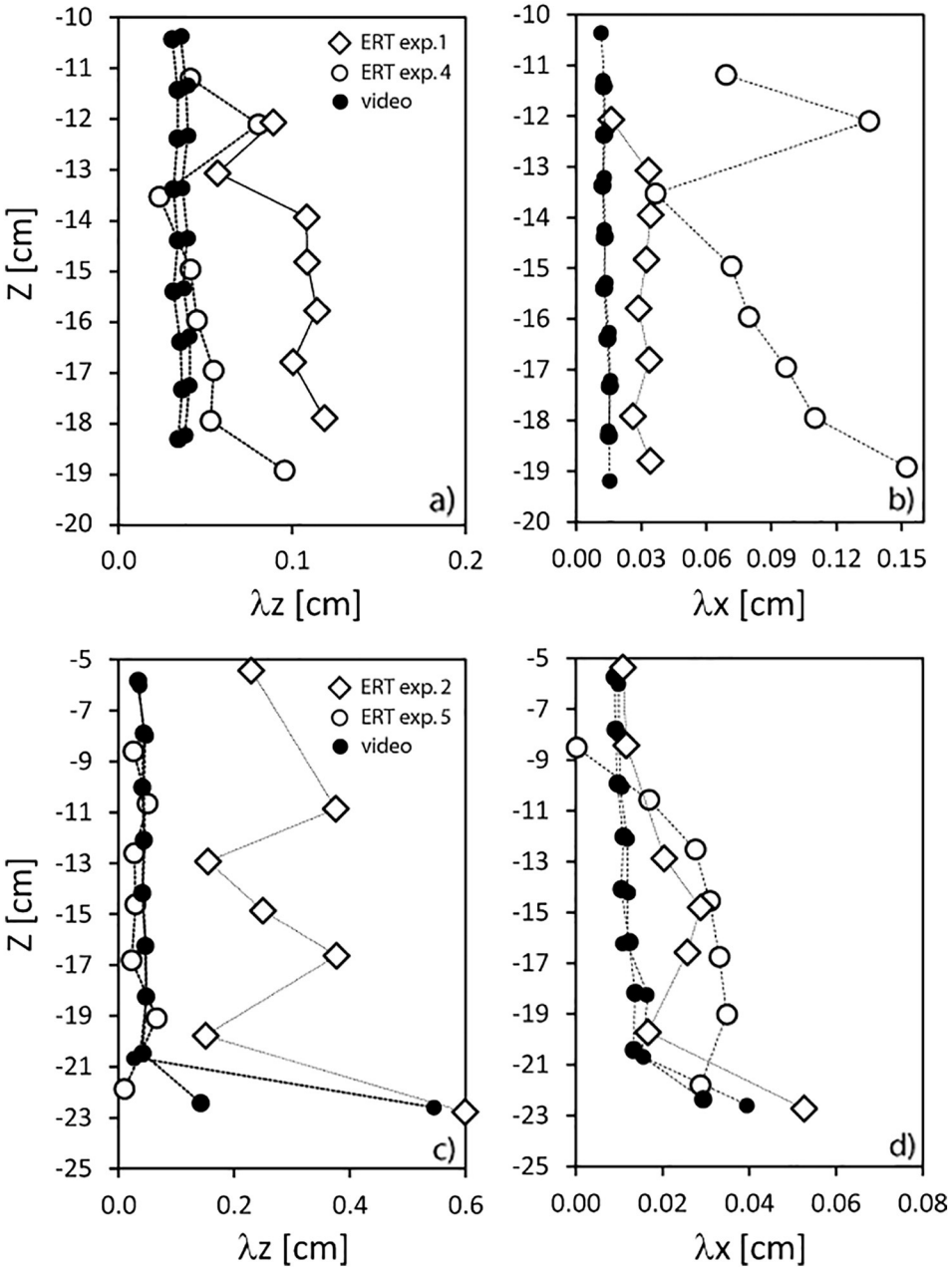

Fig. 8. Variation of the longitudinal λ_z and transverse dispersivities λ_x as function of the distance z. Diamonds are values obtained with the horizontal dipole-dipole and empty circles represent the vertical dipole-dipole sequences. ERT values presented here were obtained from an inversion constrained with a L_2-norm applied to the data.

values of ρ_b close to unity expressing no variations in the pore fluid conductivities compared to the initial background. From $t = 29$ min, the shape of the tracer plume started to be fully recovered with ρ_b varying from 0 in the centre of mass to 1 at the interface with the resident fluid. The temporal evolution of the resistivity contours agree with the video analysis demonstrating the upward motion of the tracer plume until $t = 57$ min. At this stage the video reveals that the plume had not reached the outlet while the model shows around 80% of resistivity changes from top to $Z = -13$ cm. After the plume crossed the full height of the porous medium at $t = 68$ min, no resistivity contrasts attributed to possible residual concentrations of tracer were noticeable by the ERT at the scale of the model discretisation, assuming a return to full saturation by the resident fluid.

A general comparison with the video analysis highlights that the inversion contributed to smooth the resistivity contrasts particularly at the interface with the resident fluid. This smoothing effects prevented the full recovery of the shape of the plume by providing diffuse contours. Furthermore, at the centre of mass of the plume ρ_b was close to 0 only when the plume reached the centre part of the medium and then increased again toward the outlet. The data background regularization suppressed the constant resistive background noise mainly inferred by the boundary effects. Nevertheless, the resistivity contrasts attributed to the shape of the tracer plume were perturbed in the lower and upper parts of the medium. The RMS errors were inferior to 2% for the whole time series but inversion results were only reliable when the plume was located in the centre part of the bead pack. Reasons involving these inaccuracies will be discussed later on.

4.2. Quantification of the tracer vertical velocity

The vertical average velocities estimated from the adjustment of the temporal displacement of the centre of mass z_p are shown in Fig. 5a. ERT measurements were sensitive to the average pore velocities imposed by the pump v_{pump}, but horizontal and vertical sequences as well as the type of norm (L_1 and L_2) do not present noticeable differences in v_z estimation. For both arrays v_z was always found lower than v_{pump} by 20%, while values obtained from the video analysis exhibited the same trend but average v_z were lower than v_{pump} by 30 to 40%. The relative local velocities estimated from Eq. (14) for each time step followed the same trend as the video analysis in areas where the shape of the tracer plume was fully recovered by the inversion procedure (Fig. 6). However, some points clearly differed from the general trend like at $Z = -13$ cm of experiment 4 where v_z increased by 50%. Such local variations were related to measurement errors and convergence problems in the inversion procedure of the corresponding time serie.

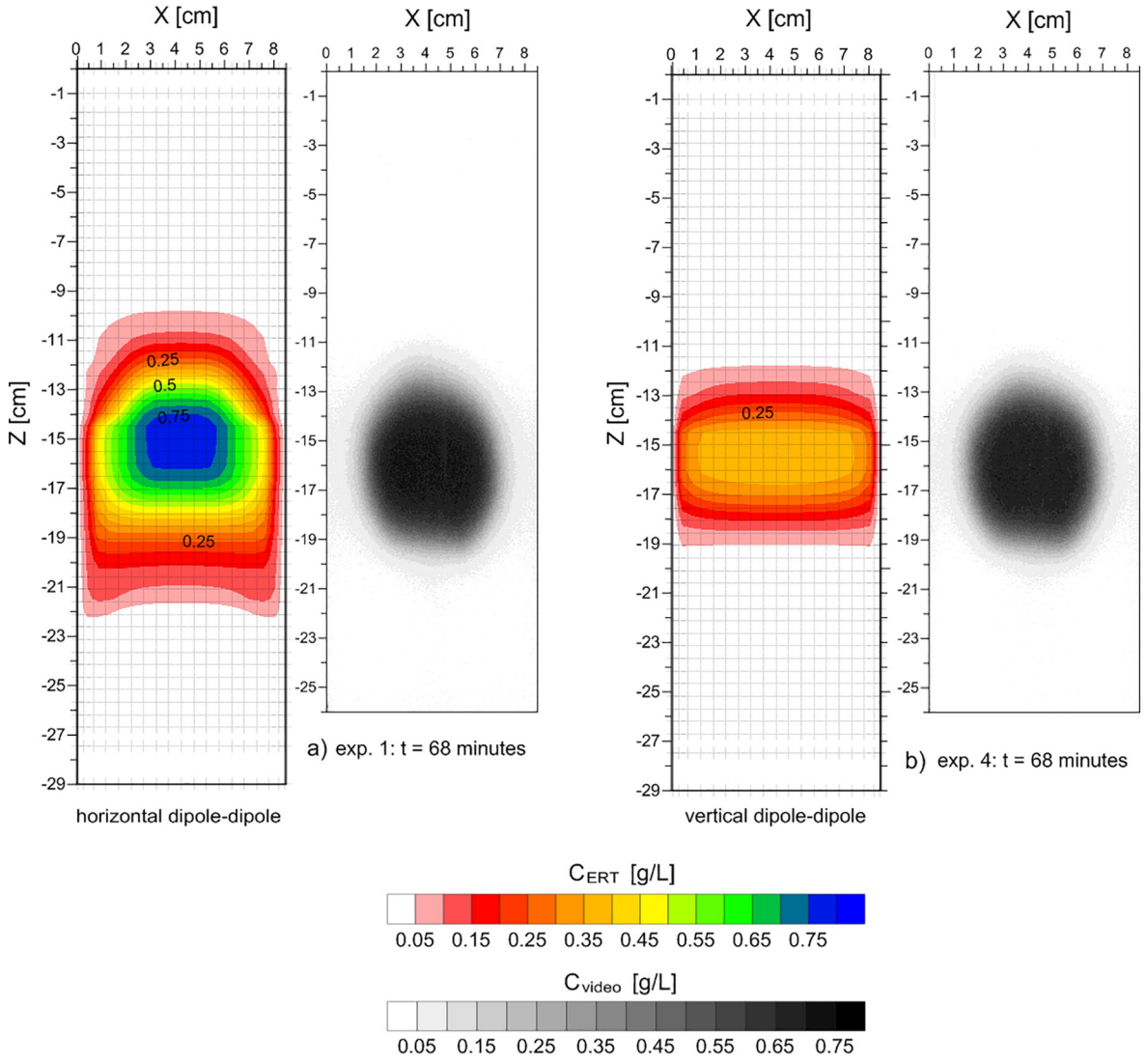

Fig. 9. Comparison of the reconstructed 2D concentration contours of the tracer plume from horizontal (a) and vertical (b) dipole dipole at $t = 68$ min for a L_2-norm applied to the data.

The agreement between the two methods shows that the underestimations of the vertical velocity were not related to the ERT procedure but due to physical phenomena. Quantification of these differences was expressed through the retardation factor $R_f = v_{pump}/v_z$ in Fig. 5b. For ERT we found an average $R_f = 1.14$ slightly decreasing with the pore velocity imposed by the pump. Retardation of the dye shows the same trend but with a slightly higher retardation factor $R_f = 1.24$. These results agree with previous studies (Peters et al., 1996) reporting values of $R_f = 1.1$ for NaCl with similar flow conditions in unconsolidated sands. The leading processes to explain this retardation difference between the ERT and the video analysis could not be confirmed at the pore volume scale investigated. However, an alternative saturation experiment of the tracer conducted in a fully dried bead pack with a permeability lower by one order of magnitude revealed that the dye saturation front progressed slower than the water saturation front (Lekmine et al., 2012). Then the higher values of the retardation factor estimated from the video analysis compared to the ERT could be explained by the different physico-chemical properties between NACl and the dye. The dissolved methyl blue is a large molecule of triarylmethane isomers having a particular affinity with the charged surface. In these conditions the retardation may be attributed to adsorption on the specific surface of the non-treated glass beads used for our 7 experiments (Table 1). Furthermore, the alternative experiment performed by Lekmine et al. (2012) highlighted that due to its relatively high molecule size, compared to Na^+ and Cl^-, the propagation of the methyl blue in the flow direction is slown down in areas with smaller permeabilities.

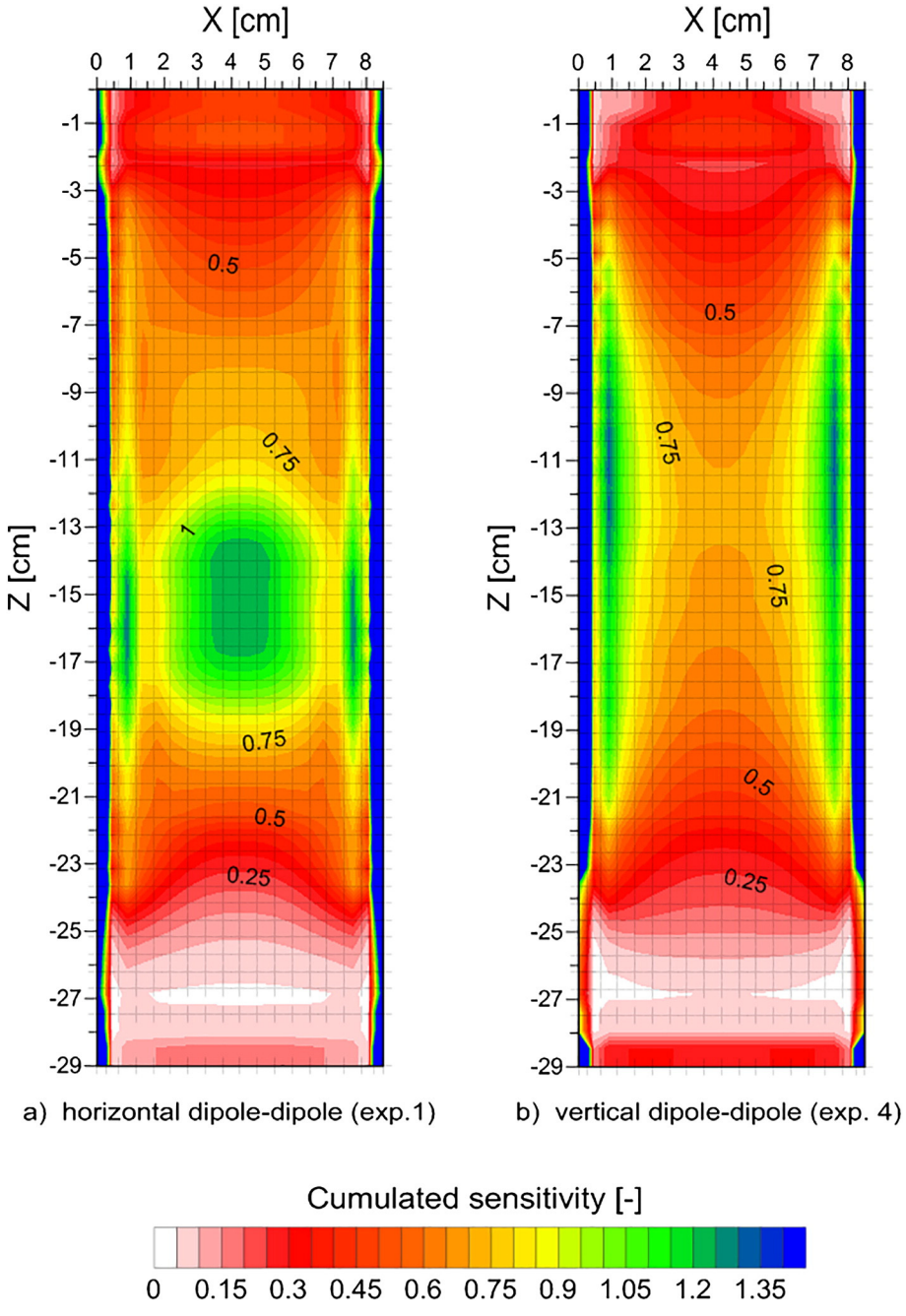

Fig. 10. Electrical sensitivity calculated from the sum of the squared Jacobian matrix J^TJ (Eq. (7)) for each model cell at the last iteration of the inversion models established from the 210 measurements acquired in horizontal (a) and vertical (b) dipole-dipole respectively for experiments 1 and 4 at $t = 68$ min.

4.3. Dispersion parameters

The experiments described in Table 1 were performed under different flow rates and repeated for each array in order to test the reliability of the ERT to quantify the mixing processes of the tracer. Longitudinal (D_z) and transverse (D_x) dispersion coefficients were quantified by fitting video and ERT concentrations (Fig. 4) with the analytical solution provided in Eq. (14). Fig. 7a presents the normalised longitudinal dispersion coefficients D_z/D_m for experiments 1 to 7 deduced from ERT and their corresponding video analysis as function of the Péclet number. Dispersion coefficients varied from 8 to 200 showing that mechanical dispersion was dominant in respect of molecular diffusion. Results from the seven video analysis are close to the theoretical curve extracted from Bachmat (1968) with D_z/D_m linearly increasing from 18 to 100. The 4 experiments monitored with the vertical dipole-dipole provided longitudinal dispersion coefficients in agreement with the video analysis and the theoretical curve. However, values estimated from horizontal dipole-dipole measurements overpredicted the dispersion coefficient by at least a factor two. These observations are confirmed by the vertical distribution of the longitudinal dispersivity (Fig. 8). Video analysis for experiments 1 and 4, performed under the same experimental conditions, were constant during the tracer propagation and both returned identical average values of $\lambda_z = 0.04$ cm for $-10 < Z < -19$ cm (Fig. 8a). The estimation inferred by the vertical dipole-dipole was in the same range with $\lambda_z = 0.043$ cm whilst the average deduced from the horizontal dipole-dipole was almost 3 times higher with $\lambda_z = 0.11$ cm. Results from experiments conducted with a higher flow rate $Q = 1.5$ mL/min (Fig. 8c), present the same behaviour in the same range of dispersivity.

Experiments monitored with the horizontal dipole-dipole sequence demonstrated that this array was more reliable to evaluate the transverse dispersivity (Fig. 7b). Transverse dispersion coefficients D_x/D_m also varied linearly with the Péclet number on a range of $4 < D_x/D_m < 300$. But only the horizontal dipole-dipole sequence inverted with an L_2-norm applied to the data was able to return values close to the dispersion coefficient found with the video analysis. Conversely, the vertical dipole-dipole overestimated the dispersion coefficient by a factor between 2 and 10. The vertical distribution of λ_x also confirmed that the horizontal dipole-dipole was more suitable but still slightly overestimates the video analysis (Fig. 8b and d).

These differences between both arrays in the quantification of the longitudinal and transverse dispersion are highlighted in Fig. 9. The 2D concentration fields obtained from the video and the ERT at $t =$ 68 min are compared for experiments 1 and 4 (Table 1). Although the horizontal dipole-dipole sequence mostly retrieved the shape of the plume, C_{ERT} contours were strongly smoothed, particularly in the flow direction which contributed to an overestimation of D_z/D_m (Fig. 9a). The vertical dipole-dipole sequence provided less smoothed vertical concentration contours (Fig. 9b) which in turn give values of D_z/D_m close to those found by the video (Fig. 7a). However, this array did not correctly restore the horizontal shape of the plume. The concentration in the vicinity of the centre of mass of the plume, $C_{ERT} = 0.35$ mg/L, was twice lower than the injected concentration (0.75 mg/L) also recovered by video.

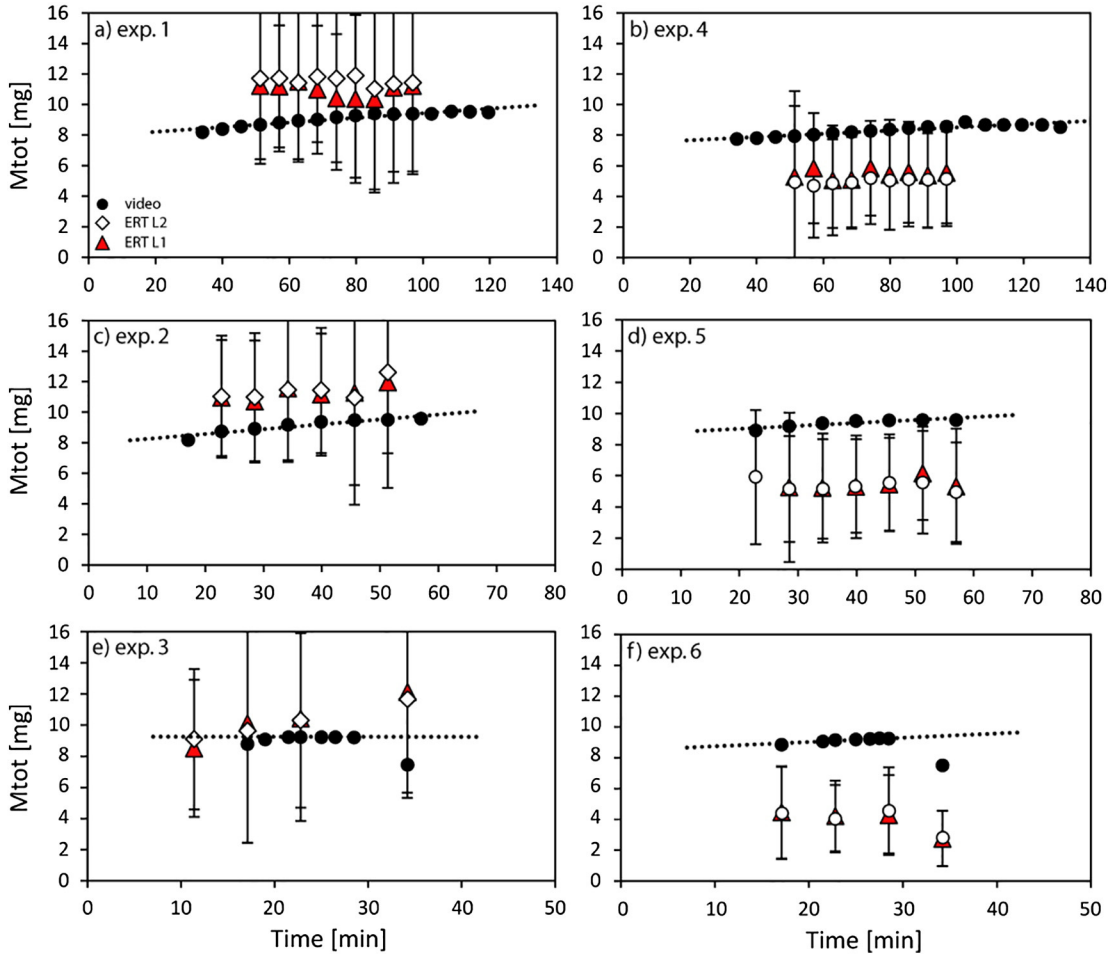

Fig. 11. Total mass of tracer recovered from integration of the 2D C_{ERT} and C_{VIDEO} concentrations (Eq. (16)) for experiments 1 to 6. For each time series presented here the full shape of the tracer plume was recovered by the 2D ERT inversion and video analysis. Experiments 1 to 3 were performed with the horizontal dipole-dipole sequence and experiments 4 to 6 with the vertical dipole-dipole sequence.

The distribution of the cumulated 2D electrical sensitivity for the two inverted time series (Fig. 10) demonstrated that the horizontal dipole-dipole had higher values in the centre part of the medium and was particularly sensitive to the presence and the shape of the plume while the vertical dipole-dipole was horizontally insensitive, returning overestimated transverse dispersion coefficients. Both sequences presented high sensitivity values for cells close to the boreholes while they varied from low to negligible near the inlet and outlet. These lower local sensitivities highlighted the lack of local measurements with small and intermediate spacings in areas not covered by electrodes, providing a weak response when the tracer was nearby the inlet and outlet. This limited the reliable recovery of the tracer resistivity contrasts only in the centre part of the medium meanwhile the inverse modelling was not able to reconstruct the shape of the tracer close to the inlet and outlet (Fig. 3).

4.4. Total mass recovery

The total mass of tracer recovered for each experiment was estimated by integrating the entire ERT concentrations C_{ERT} of each two-dimensional section and the renormalised video concentrations C_{VIDEO} (Eq. (16)). The total volume of tracer injected, $V_{tot} = 11$ mL, was identical for all experiments corresponding to a total mass $M_{tot} = 8.5$ mg. The mass estimated by the video analysis was very close to the total mass of tracer injected showing steady values increasing slightly from 8 to 9.5 mg over the investigated duration of experiments 1 to 6 (Fig. 11). These temporal rises represented 17% of the total mass recovered over the time and mainly affected experiments 1 and 2. Results obtained from ERT concentrations showed that measurements performed with the horizontal dipole-dipole sequence always overestimated the total mass of tracer by 35, 39 and 22% respectively for experiments 1 to 3 (Fig. 11). On the contrary, the dipole-dipole vertical sequence underestimated the mass on average by −42, −36 and −46% respectively for experiments 4 to 6.

Oldenborger et al. (2007a) showed from field experiments that for both array types ERT imaging consistently underpredicted tracer mass recovery and that the vertical dipole-dipole provided better estimates. Here results were correlated to the observations previously made from Fig. 9 underestimating the ERT concentrations in the centre of mass of the plume by nearly 50% for the vertical dipole-dipole while the horizontal dipole-dipole overestimated C_{ERT} in the centre of mass of the plume and at the interface with the resident fluid. This demonstrated that for both sequences the distribution of the cumulated sensitivity in presence of the tracer plume greatly influenced the inverted resistivity ratios (Fig. 3) and the consecutive total mass recovered. Inversion of the horizontal dipole-dipole sequence favoured longitudinal smoothing of the resistivity contrast at the interface and produced unrealistic low resistivity at the centre of mass, returning concentrations over the maximal tracer concentration $C_t = 0.75$ g/L. Then the recovered mass of tracer integrated on the full sections were also overestimated compared to the video analysis (Fig. 11a to c). This behaviour was somewhat expected due to the inability of the least-square smoothness constrained method to recover sharp conductivity contrasts, enhanced by the mesh discretization and the geometry of the medium. On the contrary, the vertical measurement sequence was significantly less sensitive to the presence of the tracer plume (Fig. 10b), returning underestimated M_{tot} for experiments 4 to 6 (Fig. 11d to f).

4.5. Influence of the petrophysical parameters

For most of the experiments, the total mass discrepancies between ERT and the video analysis remained within the error bars (Fig. 11) also taking into account uncertainties related to the formation factor (Eq. (3)). The disadvantage of using a petrophysical relationship to link the modelled bulk resistivities ρ_b to the ERT concentrations introduced more uncertainties in the quantification of the dispersion coefficients and the total mass recovered. In our experimental conditions, errors inferred by the formation factor were minimized compared to other laboratory (Wehrer and Slater, 2015) or field studies (Singha and Gorelick, 2005) since the tests were here performed in homogeneous bead packs, fully water saturated ($Se = 1$) and with well-known conductivities of the background resident fluid and tracer (Table 1).

Fig. 12 illustrates the sensitivity of the total mass recovered and the longitudinal dispersion coefficient D_z/D_m for experiment 1 at $t = 68$ min in regards to variation of the cementation factor m and the porosity ϕ. Their sensitivity to m and ϕ was tested successively by changing, for instance, the value of m between −25 and +25% from the initial set ($m = 1.3$, $\phi = 0.36$) while ϕ was kept constant. The initial values provided an ERT estimation of $M_{tot} = 11.5$ mg which was 35% higher than the actual mass injected (Fig. 11). The longitudinal dispersion coefficient was also overestimated in respect of the video analysis and the theoretical curve of Bachmat (1968) with $D_z/D_m = 22$ (Fig. 7a). The recovery of the actual mass $M_{tot} = 8.5$ mg required to decrease m by −10% or raise ϕ by +11% returning values of $m = 1.2$ or $\phi = 0.41$. Similarly, adjustment of D_z/D_m with the video analysis required to lower m by −15% or increase ϕ by +15% returning $m = 1.1$ or $\phi = 0.41$. This value of the porosity was not realistic since it was

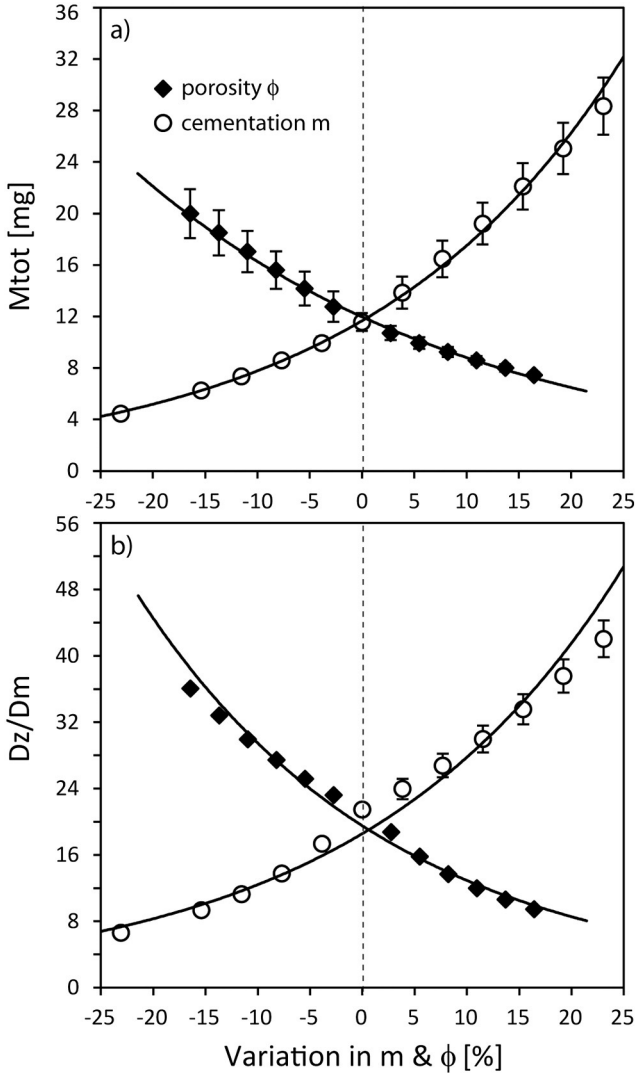

Fig. 12. Influence of the cementation factor and porosity (Eq. (3)) on the estimation of the total mass of tracer recovered by ERT in a), and the longitudinal dispersion coefficient D_z/D_m in b) for experiment 1 at $t = 68$ min. 0% correspond to the initial set of parameters $m = 1.3$ and $\phi = 0.36$.

experimentally quantified to 0.36 ± 0.01. However, the cementation factor initially chosen from the literature Archie (1942), returned here $m = 1.1$ and 1.2 which were also in agreement with values reported by Friedman (2005) for glass bead packs in the same porosity ranges. These results highlighted that small errors of these empirical parameters can also contribute to non-negligible wrong estimates in the quantification of solute transport parameters and the total mass recovery. Hence, for our simplified conditions a variation of m or ϕ by 8% implies 30% and 40% changes in D_z/D_m and M_{tot} respectively.

5. Discussion and conclusions

This work intended to evaluate the reliability of time lapse cross-borehole ERT measurements to quantify the 2D transport parameters and the total mass recovery of saline tracers in porous media. It also provided an insight of the uncertainties inferred by the array types, the sequences of selected quadripoles in relation to the tracer plume geometry as well as the influence of the structural parameters used to calibrate the petrophysical relationships. A 2D functional experimental design was developed from bead packs in which the spread of dyed tracers was monitored by ERT imaging and video analysis. For these particular experimental conditions, the horizontal and vertical dipole-dipole sequences were both sensitive to the vertical pore velocity and captured the retardation inferred by the tracer absorption on the particles. The total mass of tracer recovered was always overestimated by the horizontal dipole-dipole and underestimated by the vertical dipole-dipole. The vertical dipole-dipole was reliable to quantify the longitudinal dispersion, while the horizontal dipole-dipole returned better estimation for the transverse dispersion. Differences were influenced by the smoothing character of the least-square inversion method. Also, the cumulated 2D sensitivity sections in relation to the distribution of plume's fluid conductivity demonstrated that in such laboratory conditions the reliability of the results were also constrained by the geometry and dimensions of the experiment. Here the experimental design was constrained to 2D hydrodynamic conditions where the 2D tracer plumes were assumed to spread in the ERT image plane. In these conditions the 2.5 forward modelling strategy of the regularised time series (Eq. (2)) allowed to retrieve the shape and resistivity changes attributed the tracer propagation. However, for such important resistivity contrasts between the tracer and the medium even slight deviation from the image plane may result in false resistivity changes as seen in the centre of mass of the tracer at $t = 46$ min (Fig. 3). Although the errors incurred might be small, they constitute supplementary additive errors in the quantification of the dispersion parameters (Fig. 7) and the total mass of tracer recovered M_{tot}. Shadow effects (Nimmer et al., 2008) must be then consider with the 2D sensitivity sections and the uncertainties on the petrophysical parameters to explain the differences with the video analysis in the M_{tot} recovery (Fig. 11).

These outcomes demonstrated that in field situations ERT cross-borehole investigations must be performed in 3 dimensions to avoid misleading interpretations about the size, shape and location of solutes and contaminant plumes in groundwater. However, upscaling to 3D field conditions also requires the establishment of prior information to accurately quantify the mass and transport parameters. Our results highlighted that appropriate estimation of the dispersion parameters would be significantly improved from prior knowledge of the shape, location and physico-chemical properties of the tracer or contaminant involved. This is a first step to optimize the choice of the sequence of time-lapse ERT measurements and its updates for each time series (Bellmunt et al., 2016). Furthermore, even for our simplified experimental conditions wrong characterisation of some petrophysical parameters can lead to non-negligible errors in mass and transport processes estimation. In field conditions any relevant prior information about the type and distribution of heterogeneities, such as fracture networks and permeability changes, must be considered since preferential flows or flow bypassing may occur in particular directions, where the ERT measurement sequence shows low cumulated sensitivities. This would help to better calibrate the chosen petrophysical relationships linking the bulk to the local fluid resistivities.

Acknowledgments

This research was financially supported by the University Paris-Sud under the research fund "*Modelling physical processes in Earth Sciences*". The authors give special thanks to the Measurement Platform PEPS, R. Pidoux for improvements made in the experimental design and A. Aubertin for the data acquisition software. We also thank Benoit Semin, Kaveh Sookhak Lari, and the anonymous reviewers for their helpful comments and suggestions.

References

Archie, G.E., 1942. The electrical resistivity log as an aid in determining some reservoir characteristics. Soc. Pet. Eng. 146 (1), 54–62.
Bachmat, Y., 1968. On the similitude of dispersion phenomena in homogeneous and isotropic porous medium. Water Resour. Res. 4, 1079–1083.
Bellmunt, F., Marcuello, A., Ledo, J., Queralt, P., 2016. Capability of cross-hole electrical configurations for monitoring rapid plume migration experiments. J. Appl. Geophys. 124, 73–82.
Bevc, D., Morrison, H.F., 1991. Borehole to surface electrical resistivity monitoring of salt water injection experiment. Geophysics 56, 769–777.
Bing, Z., Greenhalgh, S.A., 2000. Cross-hole resistivity tomography using different electrode configurations. Geophys. Prospect. 48, 887–912.
Binley, A., Henry-Poulter, S., Shaw, B., 1996. Examination of solute transport in an undisturbed soil column using electrical resistance tomography. Water Resour. Res. 32, 763–769.
Chambers, J.E., Wilkinson, P.B., Weller, A.L., Meldrum, P.I., Ogilvy, R.D., Caunt, S., 2007. Mineshaft imaging using surface and crosshole 3D electrical resistivity tomography: a case history from the East Pennine Coalfield, UK. J. Appl. Geophys. 62, 324–337.
Charette, V.J., Evangelista, E., Chertcoff, R., Auradou, H., Hulin, J.-P., Ippolito, I., 2007. Influence of disorder on solute dispersion in a flow channel. Eur. Phys. J. Appl. Phys. 39, 267–274.
Daily, W., Ramirez, A., 1995. Electrical resistance tomography during in-situ trichloroethylene remediation at the Savannah River Site. J. Appl. Geophys. 33, 239–249.
Daily, W., Ramirez, A., LaBrecque, D., Barber, W., 1995. Electrical resistance tomography experiments at the Oregon Graduate Institute. J. Appl. Geophys. 33, 227–237.
Day-Lewis, F.D., Harris, J.M., Gorelick, S.M., 2002. Time-lapse inversion of crosswell radar data. Geophysics 67 (6), 1740–1752.
Friedman, S.P., 2005. Soil properties influencing apparent electrical conductivity: a review. Comput. Electron. Agric. 46, 45–70.
Furman, A., Ferré, T.P.A., Warrick, A.W., 2004. Optimization of ERT surveys for monitoring transient hydrological events using perturbation sensitivity and genetic algorithms. Vadose Zone J. 3, 1230–1239.
Furman, A., Ferré, T.P.A., Health, G.L., 2007. Spatial focusing of electrical resistivity surveys considering geologic and hydrologic layering. Geophysics 72, F65–F73.
Garré, S., Koestel, J., Guenther, T., Javaux, M., Vanderborght, J., Vereecken, H., 2010. Comparison of heterogeneous transport processes observed with electrical resistivity tomography in two soils. Vadose Zone J. 9, 336–349.
Guyon, E., Hulin, J.P., Petit, C., Mitescu, C.D., 2001. Physical Hydrodynamics. Oxford University Press.
Hayley, K., Bentley, L.R., Pidlisecky, A., 2011. Simultaneous time-lapse electrical resistivity inversion. J. Appl. Geophys. http://dx.doi.org/10.1016/j.jappgeo.2011.06.035 11pp.
Herrera, G.S., Pinder, G.F., 2005. Space-time optimization of groundwater quality sampling networks. Water Resour. Res. 41, W12407. http://dx.doi.org/10.1029/2004WR003626.
Kim, K.H., Lee, K.K., 2007. Optimization of groundwater-monitoring networks for identification of the distribution of a contaminant plume. Stoch. Environ. Res. Risk Assess. 21 (6):785–794. http://dx.doi.org/10.1007/s00477-006-0094-x.
Koestel, J., Kemna, A., Javaux, M., Binley, A., Vereecken, H., 2008. Quantitative imaging of solute transport in an unsaturated and undisturbed soil monolith with 3-D ERT and TDR. Water Resour. Res. 44, W12411.
Koestel, J., Vanderborght, J., Javaux, M., Kemna, A., Binley, A., Vereecken, H., 2009a. Noninvasive 3-D transport characterization in a sandy soil using ERT: 1. Investigating the validity of ERT-derived transport parameters. Vadose Zone J. 8:711–722. http://dx.doi.org/10.2136/vzj2008.0027.
Koestel, J., Vanderborght, J., Javaux, M., Kemna, A., Binley, A., Vereecken, H., 2009b. Noninvasive 3-D transport characterization in a sandy soil using ERT: 2. Transport process inference. Vadose Zone J. 8:723–734. http://dx.doi.org/10.2136/vzj2008.0154.
Labrecque, D.J., Miletto, M., Daily, W.D., Ramirez, A., Owen, E., 1996a. The effects of noise on Occam's inversion of resistivity tomography data. Geophysics 61:538–548. http://dx.doi.org/10.1190/1.1443980.
Labrecque, D.J., Ramirez, A.L., Daily, W.D., Binley, A.M., Schima, S.A., 1996b. ERT monitoring of environmental remediation processes. Meas. Sci. Technol. 7, 375–383.
Lekmine, G., Pessel, M., Auradou, H., 2012. Experimental study of ERT monitoring ability to measure solute dispersion. Ground Water 50 (2):285–295. http://dx.doi.org/10.1111/j.1745-6584.2011.00837.
Leroy, P., Revil, A., Kemna, A., Cosenza, P., Ghorbani, A., 2008. Complex conductivity of water-saturated packs of glass beads. J. Colloid Interface Sci. 321:103–107. http://dx.doi.org/10.1016/j.jcis.2007.12.031.

Loke, M.H., 2004. Tutorial: 2-D and 3-D Electrical Imaging Surveys. Geotomo Software Pty Ltd. (136 pp.).
Loke, M.H., Barker, R.D., 1996. Rapid least-squares inversion of apparent resistivity pseudosections by a quasi-Newton method. Geophys. Prospect. 44, 131–152.
Meyer, P.D., Valocchi, A.J., Eheart, J.W., 1994. Monitoring network design to provide initial detection of groundwater contamination. Water Resour. Res. 30 (9):2647–2659. http://dx.doi.org/10.1029/94WR00872.
Meyerhoff, S.B., Maxwell, R.M., Revil, A., Martin, J.B., Karaoulis, M., Graham, W.D., 2014. Characterization of groundwater and surface water mixing in a semiconfined karst aquifer using time-lapse electrical resistivity tomography. Water Resour. Res. 50: 2566–2585. http://dx.doi.org/10.1002/2013WR013991.
Nimmer, R.E., Osiensky, J.L., Binley, A.M., Williams, B.C., 2008. Three-dimensional effects causing artifacts in two-dimensional, cross-borehole electrical imaging. J. Hydrol. 359:59–70. http://dx.doi.org/10.1016/j.jhydrol.2008.06.022.
Oldenborger, G.A., Routh, P.S., Knoll, M.D., 2007a. Model reliability for 3D electrical resistivity tomography: application of the volume of investigation index to a time-lapse monitoring experiment. Geophysics 72, 167–175.
Oldenborger, G.A., Knoll, M.D., Routh, P.S., Labrecque, D.J., 2007b. Time-lapse ERT monitoring of an injection/withdrawal experiment in a shallow unconfined aquifer. Geophysics 72, F177–F187.
Perri, M.T., Cassiani, G., Gervasio, I., Deiana, R., Binley, R., 2012. A saline tracer test monitored via both surface and cross-borehole electrical resistivity tomography: comparison of time lapse results. J. Appl. Geophys. 79, 6–16.
Peters, E.J., Gharbi, R., Afzal, N., 1996. A look at dispersion in porous media through computed tomography imaging. J. Pet. Sci. Eng. 15, 23–31.
Ramirez, A.L., Nitao, J.J., Hanley, W.G., Aines, R., Glaser, R.E., Sengupta, S.K., Dyer, K.M., Hickling, T.L., Daily, W.D., 2005. Stochastic inversion of electrical resistivity changes using a Markov Chain Monte Carlo approach. J. Geophys. Res. 110 (B2).
Revil, A., Glover, P.W.J., 1998. Nature of surface electrical conductivity in natural sands, sandstones and clays. Geophys. Res. Lett. 25 (5), 691–694.
Rucker, D.F., 2014. Investigating motion blur and temporal aliasing from time-lapse electrical resistivity. J. Appl. Geophys. 111, 1–13.
Singha, K., Gorelick, S.M., 2005. Saline tracer visualized with three-dimensional electrical resistivity tomography: field-scale spatial moment analysis. Water Resour. Res. 41, W05023. http://dx.doi.org/10.1029/2004WR003460.
Singha, K., Gorelick, S.M., 2006. Hydrogeophysical tracking of three-dimensional tracer migration: the concept and application of apparent petrophysical relations. Water Resour. Res. 42, W06422. http://dx.doi.org/10.1029/2005WR004568.
Slater, L.D., Binley, A., Brown, D., 1997. Electrical imaging of fractures using groundwater salinity change. Groundwater 35 (3), 436–442.
Slater, L., Binley, A., Cassiani, A.M., Birken, G., Sandberg, S., 2002. A 3D ERT study of solute transport in a large experimental tank. J. Appl. Geophys. 49, 211–229.
Van Genuchten, M.T., Alves, W.J., 1982. Analytical solutions of the one-dimensional convective-dispersive solute transport equation. United States Department of Agriculture, Technical Bulletin 1661.
Wehrer, M., Slater, L.D., 2015. Characterization of water content dynamics and tracer breakthrough by 3-D electrical resistivity tomography (ERT) under transient saturated conditions. Water Resour. Res. 51:97–124. http://dx.doi.org/10.1002/2014WR016131.
Wilkinson, P.B., Chambers, E.J., Lelliott, M., Wealthall, G.P., Ogilvy, R.D., 2008. Extreme sensitivity of crosshole electrical resistivity tomography measurements to geometric errors. Geophys. J. Int. 173, 49–62.
Wilkinson, P.B., Meldrum, P.J., Kuras, O., Chambers, J.E., Holyoake, S.J., Ogilvy, R.D., 2010. High-resolution electrical resistivity tomography monitoring of a tracer test in a confined aquifer. J. Appl. Geophys. 70, 268–276.